Integral experiment on bismuth slabs with D–T neutron irradiation for data validation*

Shi-Yu Zhang,[1,2] Yang-Bo Nie,[1,2,†] Yan-Yan Ding,[1] Qi Zhao,[3] Kuo-Zhi Xu,[1,2] Xin-Yi Pan,[1] Xiao-Yu Wang,[1] Bei-Bo He,[1] Hong-Tao Chen,[1] Qi Sun,[1] and Zheng Wei[2]

[1]*Key Laboratory of Nuclear Data, China Institute of Atomic Energy, Beijing 102413, China*
[2]*School of Nuclear Science and Technology, Lanzhou University, Lanzhou 730000, China*
[3]*Spallation Neutron Source Science Center, Dongguan 523803, China*

Accurate nuclear data for neutron interactions with bismuth are crucial for applications in nuclear technology and radiation protection. This paper presents a comprehensive benchmark analysis that compares experimental data obtained at multiple angles and thicknesses with simulations based on four nuclear-data libraries: CENDL-3.2, ENDF/B-VIII.0, JENDL-5, and JEFF-3.3. The experiments involved neutron-leakage measurements of bismuth at three thicknesses and six angles, along with standard sample validations. Pulse time distributions were reconstructed using the maximum likelihood expectation maximization algorithm, and a silicon-carbide detector was employed to accurately distinguish between deuterium–tritium and deuterium–deuterium reaction products. Simulation models validated using polyethylene-sample results demonstrated calculated-to-experimental (C/E) values of 1 ± 0.03, thus confirming their reliability. The analysis revealed that CENDL-3.2 exhibited the best overall agreement in the elastic scattering region. In the discrete inelastic scattering region, JENDL-5 performed best at larger angles, while JEFF-3.3 was more accurate at smaller angles. In the continuous inelastic scattering region, JEFF-3.3 demonstrated the best overall performance, with CENDL-3.2 achieving good agreement at selected angles. In the (n,2n) reaction region, ENDF/B-VIII.0 provided C/E values closest to unity, while JENDL-5 ensured better consistency across the full energy spectrum. These findings highlight the importance of selecting appropriate nuclear-data libraries and emphasize the necessity for ongoing data refinement to improve modeling accuracy.

Keywords: Benchmark experiment, Evaluated nuclear data, Bismuth, D–T neutron source

I. INTRODUCTION

Bismuth—a dense and nonradioactive heavy metal—is crucial in modern nuclear technology, particularly as a key component of lead–bismuth eutectic (LBE). LBE has been investigated extensively owing to its promising applications in advanced nuclear systems, such as Generation-IV reactors and accelerator-driven subcritical systems. In these systems, the LBE serves two functions: as a high-efficiency coolant and as an optimal spallation target [1–3]. These dual roles are facilitated by the exceptional neutronic and thermal-physical properties of bismuth, including its high neutron yield, significant neutron interaction cross-section, and excellent thermal conductivity. These characteristics are critical for maximizing neutron production and ensuring the safe and efficient operation of reactor systems. However, the accurate modeling of neutron transport in bismuth remains a significant challenge, primarily owing to persistent uncertainties and discrepancies in the current nuclear data [4]. Addressing these uncertainties is essential for improving the reliability of simulations and enhancing the performance of bismuth-based nuclear applications.

Despite the critical role bismuth in advanced nuclear applications, the nuclear data available for this element have not undergone the same level of extensive and rigorous validation as those for other essential materials, such as structural components or major actinides. Although the benchmarking of nuclear data for lead has advanced significantly, comprehensive and systematic benchmark experiments focusing specifically on bismuth remain limited [5–8]. Early research efforts, including the pioneering work by Simakov et al. in the 1990s, provide valuable initial insights based on measurements of neutron-leakage spectra from bismuth samples [9]. However, these early studies were constrained in scope and did not account for the full complexity of neutron interactions across a wide range of energies and angles. Consequently, discrepancies persist among the evaluated nuclear-data libraries, such as CENDL-3.2 [10], ENDF/B-VIII.0 [11], JENDL-5 [12], and JEFF-3.3 [13]. These inconsistencies underscore the necessity for further experimental investigations to validate and refine the current nuclear data, such that greater accuracy and reliability can be ensured in simulations involving bismuth.

Integral experiments are fundamental to the continuous assessment and enhancement of nuclear data. These experiments serve as benchmark tests that provide a robust and reliable basis for validating theoretical models and refining simulation codes. By generating high-precision experimental data that can be rigorously compared with computational predictions, integral experiments enable an iterative cycle of data refinement. This iterative process enhances the accuracy and reliability of nuclear-data libraries, which is crucial for ensuring the safety, efficiency, and optimization of diverse nuclear technologies. The China Institute of Atomic Energy (CIAE) has developed a comprehensive and sophisticated platform for performing such integral experiments [14–23]. This platform has contributed significantly to the field by providing reliable experimental benchmarks and advancing our under-

* This work was supported by the National Natural Science Foundation of China (11775311, U2167203, U2067205 and 12075105), the Research and Development Project of China National Nuclear Corporation (FD010241222552), the Continuous-Support Basic Scientific Research Project (BJ010261223282), the Major Science and Technology Projects of Gansu Province (22ZD6GB020), and the Fundamental Research Funds for the Central Universities (lzujbky-2024-jdzx10).

† Corresponding author, E-mail Address: nieyb@ciae.ac.cn

standing of neutron interactions, thereby supporting the continued improvement of nuclear-data quality.

Herein, we present a comprehensive benchmark experiment using bismuth slab samples irradiated by a 14 MeV deuterium–tritium (D–T) neutron source. Experimental measurements were conducted at six specific angles, i.e., 47°, 58°, 73°, 107°, 122°, and 133°, using the time-of-flight (TOF) technique to include an energy range of 0.8 to 16 MeV. The measurements were performed using bismuth slabs of three different effective thicknesses–5, 10, and 15 cm–achieved using two large bismuth samples measuring 30 cm × 30 cm × 5 cm and 30 cm × 30 cm × 10 cm. To evaluate the nuclear data, we performed a comprehensive analysis using calculated-to-experimental (C/E) values, thus enabling a systematic examination of discrepancies across different energy regions. The dominant reaction channels in each range were assessed by dividing the energy spectrum into distinct intervals. This detailed analysis allowed us to evaluate the contributions of various neutron interaction mechanisms, including elastic scattering, discrete inelastic scattering to separate energy levels, continuous inelastic scattering to a continuum of energy levels, and the (n, 2n) reaction. Monte Carlo simulations conducted using the MCNP-4C code [24] with data obtained from CENDL-3.2, ENDF/B-VIII.0, JENDL-5, and JEFF-3.3 libraries provided insights into the effects of these reactions on neutron transport in bismuth. The findings of this study are expected to refine nuclear data and support the development of more reliable and efficient lead–bismuth eutectic-based systems, which are essential for advancing next-generation nuclear technologies.

II. EXPERIMENT SETUP

A. Experimental Arrangement

The integral-experiment platform, as illustrated in Fig. 1, is composed of a neutron source, a sample stage with precise positioning capabilities, a sophisticated collimation system, a suite of detectors, and a digital data-acquisition setup. To enhance the accuracy of neutron-leakage measurements and effectively suppress background noise from environmental scattering, the main detector was placed in an adjacent hall. This strategic placement, combined with a multilayer collimation system, ensures that most neutrons reaching the detector originate from the sample, thereby maximizing the local effect-to-background ratio.

The neutron source utilized was a 400 kV nanosecond-pulse neutron generator housed at the CIAE. This generator accelerates deuterium ions (D^+) to approximately 300 keV, which then bombard a tritium–titanium (T–Ti) target, thereby generating neutrons with an energy of approximately 14.5 MeV via the D–T reaction. Operating at pulse frequencies of up to 1.5 MHz on the nanosecond scale, the generator provides high-quality neutron pulses that are ideal for integral experiments [25–27].

The sample stage featured a dual-axis electric platform designed to ensure the precise positioning and accurate alignment of the samples at specified angles. This capability is crucial for maintaining the consistency and reproducibility of the experimental measurements. The platform accommodated either the standard polyethylene sample (measuring 30 cm × 30 cm × 5 cm), which was employed to validate the accuracy and reliability of the experimental setup, or two large bismuth slabs, each measuring 30 cm × 30 cm × 5 cm and 30 cm × 30 cm × 10 cm. These bismuth slabs can be arranged individually or combined to provide three effective thicknesses, i.e., 5, 10, and 15 cm, thus enabling comprehensive neutron-leakage measurements across different experimental conditions. To ensure the purity and reliability of the data, all samples were subjected to a rigorous impurity analysis, which confirmed that the bismuth content exceeded 99.997%, thereby minimizing the effect of impurities on the experimental results.

The detection system comprised four main components: a primary detector, two neutron monitors, and an associated particle detector. The primary detector, i.e., a Φ2 × 2-inch EJ301 liquid scintillator, was used to measure neutron leakage from the sample. The two neutron monitors–both Φ0.5 × 0.5-inch EJ301 scintillators–are crucial for recording the pulse time distribution of the source neutrons, which is an essential parameter for the accurate analysis of the TOF spectra. The associated particle detector, which was constructed from silicon carbide (SiC), was employed to differentiate between alpha particles from the D–T reaction and protons from the D–D reaction. Because the residual deuterium on the tritium target can react with incoming deuterium ions, D–D reactions are inevitable. Therefore, an accurate evaluation of the effect of these D–D reactions on the D–T neutron source is a critical component of the experiment.

The data-acquisition system used GDDAQ (developed by Peking University), which is known for its user-friendly interface and is widely used in nuclear-physics experiments [28–30]. The system includes 16-channel Pixie-16 modules with a sampling rate of 500 MSPS and a 12-bit resolution. This fully digital setup allows the detector signals to be directly digitized and processed, thus simplifying the experimental setup by eliminating the necessity for complex analog electronics. The streamlined design ensures efficient and precise data acquisition, thereby enhancing the overall reliability of the experimental results.

B. Experimental-Data Processing

The experimental-data processing began with the extraction and analysis of the TOF spectra of bismuth and polyethylene samples measured at various angles. Considering the complex nature of neutron interactions in bismuth, an accurate and detailed description of the neutron source is crucial. The essential parameters, including the pulse time distribution, total neutron yield, and D–T/D–D reaction ratio, were meticulously characterized to enable precise normalization and ensure the fidelity of subsequent simulations. These source characteristics are vital to the modeling and interpretation of the TOF spectra, as they significantly affect the accuracy of comparisons between the experimental and simu-

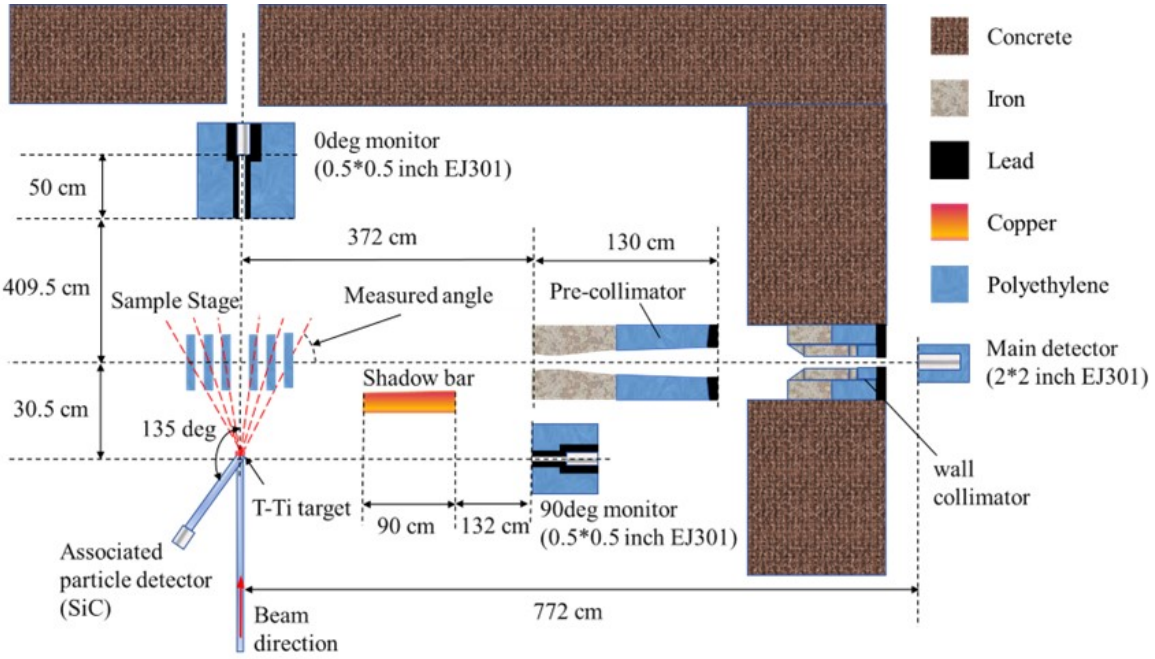

Fig. 1. (Color online) Schematic diagram of experimental setup, illustrating T–Ti neutron source, sample stage at various measured angles, shadow bar, pre-collimator, main detector, and associated particle detector.

lated results. The subsequent data-processing steps focused on addressing these critical elements to achieve reliable and meaningful outcomes.

The experiment employed the reverse TOF method, which uses the signal generated by a deuterium ion (D^+) beam passing through a pick-up ring in the accelerator tube. This pick-up signal, which was generated at a frequency synchronized with the accelerator's operating frequency of 1.5 MHz, provided a consistent timing reference. However, because most of the neutrons generated did not penetrate the sample and reach the detector, a more efficient method is required to minimize the dead time. In the reverse TOF technique, the detector signal serves as an external trigger and the pickup signal is recorded only when a neutron-detection event occurs, thereby significantly reducing the dead time and enhancing the overall efficiency of the measurements.

The zero point of the TOF spectrum was determined using the gamma-flash peak generated when the deuterium ions (D^+) interacted with the T–Ti target. Two monitoring detectors positioned at 0° and 90° relative to the beam direction were synchronized with the main detector using a shared data-acquisition system operating on a common clock. This synchronization ensured consistent timing calibration across all the detectors. Both monitoring detectors were placed directly facing the target without obstructing the structures, thus enabling the observation of clear and precise gamma-flash signals. The time-zero point for the TOF spectrum can be accurately established by subtracting the gamma flight time from these gamma-flash signals.

The main detector, a Φ2 × 2-inch EJ301 liquid scintillator, was selected for its exceptional n-gamma discrimination capability, which ensured the accurate capture of the neutron TOF spectra from the samples. Located 7.72 m from the beam extension line, the detector was calibrated using standard gamma sources (^{137}Cs and ^{207}Bi) at three energy points (0.667, 0.57, and 1.063 MeV). The energy-scale curve of the main scintillator detector was fitted by $E = 0.00187 \times chn - 0.16183$, where chn is the number of channels. Figures 2(a) and 2(b) illustrate the experimental energy spectra and calibration fitting results, respectively.

For particle discrimination, the pulse-shape discrimination (PSD) method was employed to effectively separate neutrons from gamma rays. The pulse-shape discrimination charge-to-digital converter (PSD-QDC) plot (see Fig. 2(c)) illustrates this technique, with gamma signals—clearly separated by a distinct boundary line—appearing on the left and neutron signals on the right. Neutron signals corresponding to proton-energy depositions exceeding 143 keV were isolated to generate a neutron TOF spectrum (see Fig. 2(d)). This energy threshold ensures that neutrons with a minimum energy of approximately 0.8 MeV are accurately measured. Notably, the 143 keV value refers to the energy deposited by protons from neutron interactions, not the energy of the neutrons. The gamma-flash peak near 30 ns was effectively excluded from the neutron TOF spectrum, and more than 99.5% of the gamma events were successfully eliminated, thereby ensuring reliable n-gamma discrimination.

The final TOF spectrum was constructed via a normalization process incorporating the detector efficiency and neutron yield measurement, as follows:

$$TOF_{\text{final}} = \frac{TOF_{\text{in}} \times \varepsilon_{\text{eff}}}{K \times N_{\alpha} \times S} = \frac{TOF_{\text{OUT}}}{N_{\text{n}} \times S} \tag{1}$$

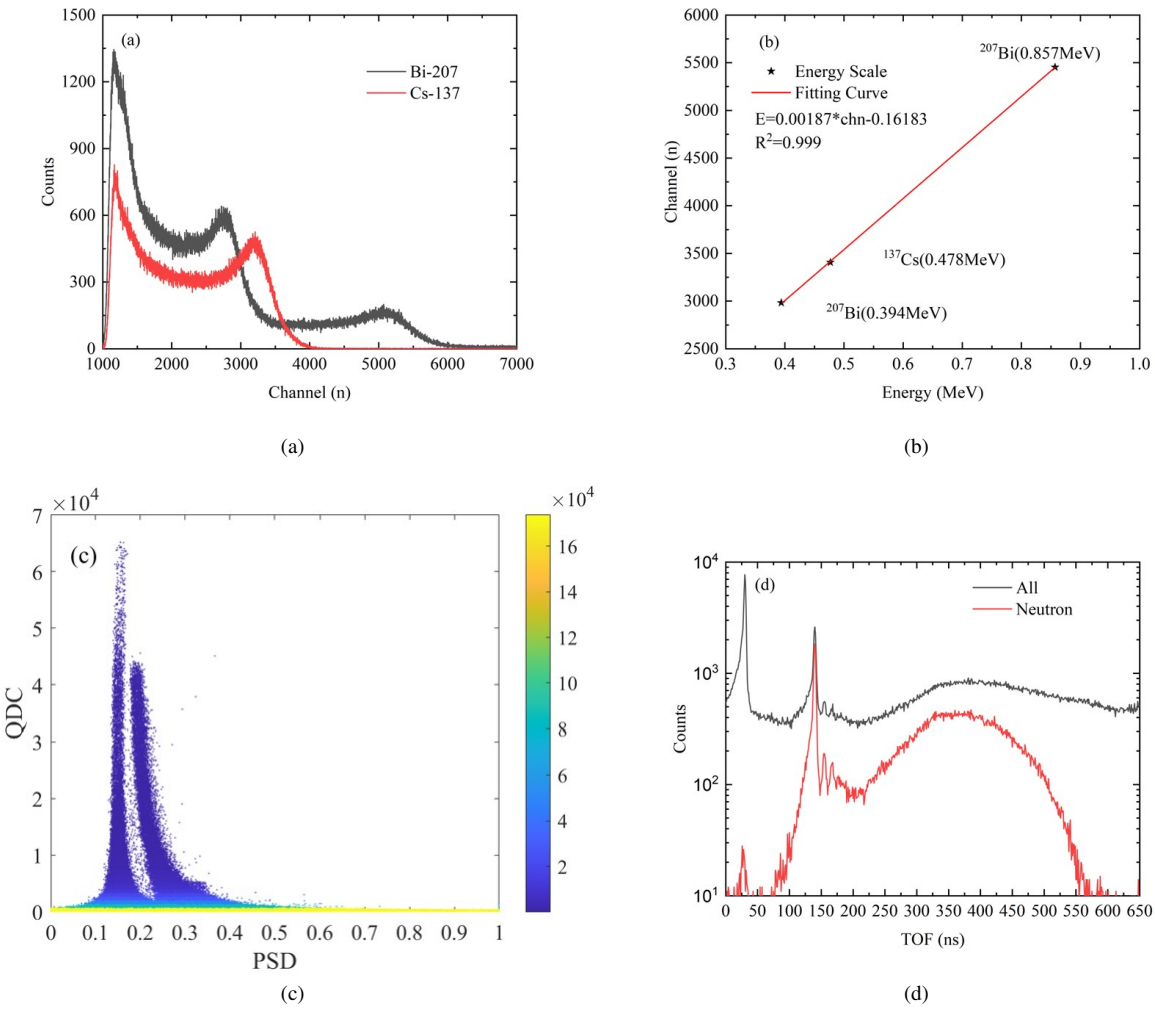

Fig. 2. (Color online) (a) and (b) show calibration results of main detector. (c) presents n-gamma discrimination capability, and (d) displays TOF spectra after applying PSD-based discrimination.

Here, TOF_{in} represents the actual neutron spectrum entering the detector and ε_{eff} denotes the detector efficiency. The coefficient K was used to calculate the neutron yield based on the accompanying particle method. N_α refers to the number of alpha particles detected and S denotes the effective area of the detector. TOF_{OUT} represents the output TOF spectrum and N_{n} represents the total count of the neutron source. The final TOF spectrum is presented as the probability of detecting a neutron per unit of emitted neutrons, normalized by the effective detection area.

Accurate characterization of the pulse time distribution and neutron yield, including the D–T to D–D reaction ratios, is crucial for processing and interpreting the experimental results. The neutron yield was calculated using the associated particle method, where a SiC detector was used to analyze the energy spectrum of the accompanying particles. As shown in Fig. 3, this spectrum distinctly separates alpha particles from the D–T reaction and protons from the D–D reaction, thus enabling the precise discrimination and quantification of both reaction channels.

The neutron fluxes from both the D–T and D–D reactions were determined using the associated particle method with a SiC detector positioned at 135° and 90 cm from the target. For the T(d,n)^{4}He reaction, the flux of neutrons emitted at an angle θ was inferred from the detected alpha-particle count N_α using the following equation:

$$\Phi_{\text{n}}(\theta, E_{\text{d}}) = \frac{N_\alpha}{\Delta\Omega_\alpha} A_\alpha, \tag{2}$$

where $\Delta\Omega_\alpha = \pi r^2/R^2$ is the solid angle subtended by the SiC detector, with $r = 0.16$ cm and $R = 90$ cm; and $A_\alpha = 1.263$ is the anisotropy correction factor corresponding to $E_{\text{d}} = 147$ keV and an emission angle of 135°. The total neutron yield N_{n} is related to the flux as follows:

$$\frac{\Phi_{\text{n}}(\theta, E_{\text{d}})}{N_{\text{n}}} = \frac{\sigma(\theta)}{\sigma_{\text{tot}}}, \tag{3}$$

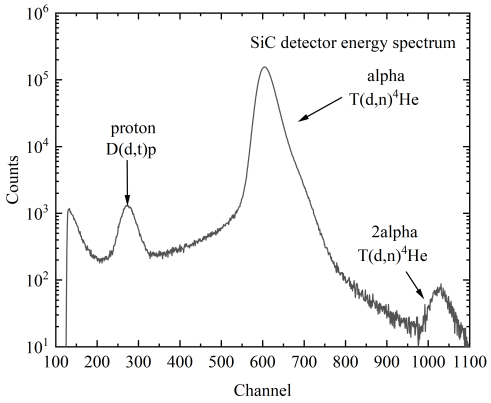

Fig. 3. Energy spectrum obtained from SiC detector (associated particle detector), which clearly shows the effective separation between protons and alpha particles.

where $\sigma(\theta) = 0.336$ b is the differential cross-section at $\theta = 0^\circ$ and $\sigma_{\text{tot}} = 3.984$ b is the total cross-section of the T(d,n)^{4}He reaction. Substituting the relevant parameters yielded a conversion factor of 1.576×10^6 neutrons per alpha particle detected.

Similarly, for the D(d,n)^{3}He reaction, protons detected from the competing D(d,p)T reaction were used to infer the neutron flux as follows:

$$\phi(\theta, E_{\text{d}}) = \frac{N_{\text{p}}}{\Delta\Omega_{\text{p}}} A_{\text{p}}, \tag{4}$$

where N_{p} denotes the measured proton count, $\Delta\Omega_{\text{p}}$ denotes the solid angle of the detector, and $A_{\text{p}} = 2.3412$ denotes the anisotropy factor. Because the D(d,p)T and D(d,n)^{3}He reactions involve different channels, their yields are related but not exactly equal; a conversion factor based on the ratio of the differential cross-section at 0° to the total cross-section is applied. The total neutron yield N_{n} was obtained as follows:

$$\frac{\phi(\theta, E_{\text{d}})}{N_{\text{n}}} = \frac{\sigma(0)}{\sigma_{\text{tot}}}, \tag{5}$$

where $\sigma(0) = 5.56$ mb is the differential cross-section at 0° and $\sigma_{\text{tot}} = 35$ mb. The resulting conversion factor between the detected proton count and total neutron yield was 1.551×10^6.

These calculations enable the accurate normalization of neutron yields as well as the real-time monitoring of the neutron source strength for both reaction channels.

The neutron pulse time distribution was reconstructed from the neutron TOF spectra measured using the monitoring detectors. The neutron TOF spectra were specifically selected for this reconstruction because of their low background noise, which enhanced the accuracy and precision of the results. The measured neutron TOF spectra were mathematically correlated with the neutron pulse time distribution through a response matrix. This matrix represents the relationship between the times at which neutrons were generated and their corresponding TOF spectra recorded by the monitors.

The reconstruction utilizes the maximum likelihood expectation-maximization (MLEM) algorithm [31], which requires an input spectrum to begin the iterative procedure. Therefore, the TOF spectrum of the gamma peak recorded by the monitoring detectors was selected as the initial spectrum. Subsequently, the MLEM algorithm iteratively refines the neutron pulse time distribution, thus optimizing the convergence and reducing the computational complexity. This method ensures a precise and reliable reconstruction, which is essential for accurate neutron transport analysis [32].

The response matrix—constructed through Monte Carlo simulations using the MCNP-4C program and TARGET software [33]—models neutron transport and the energy and angular distribution of the source (see Fig. 4). This matrix spans a TOF window of -200 ns to +200 ns, with a fine bin width of 0.1 ns for precise resolution. Figure 4 shows the neutrons emitted at different times that contribute to the response matrix. The reconstructed pulse time distribution shown in Fig. 4(c) shows excellent agreement with the experimental TOF spectra. Furthermore, Fig. 4(d) illustrates the variations in the pulse time distribution under different experimental conditions, thus effectively capturing the changes and confirming the robustness of the reconstruction method.

C. Experimental Uncertainty Analysis

The final uncertainties in the experiment were attributed to several key sources [34]. The statistical uncertainty in the measurement of the neutron source TOF remained at $\leq 0.5\%$, whereas the statistical uncertainty in the alpha particle measurements was limited to $\leq 0.2\%$. The relative detection efficiency uncertainty contributed up to 3%, and the statistical uncertainty in the neutron count for each channel was controlled closely. These combined uncertainties were systematically considered in the data analysis to ensure the reliability and accuracy of the experimental results.

III. MONTE CARLO SIMULATION

Simulations are vital to benchmark studies as they provide the calculated (C) values necessary for a meaningful comparison with experimental (E) measurements. In this study, the MCNP code was employed to simulate neutron TOF spectra using nuclear data from several evaluated libraries. These simulations are critical for replicating the experimental conditions with high fidelity and for ensuring that comparisons between the measured and simulated results are robust and reliable.

The accuracy of the simulation model depends significantly on the detailed and precise characterization of the neutron source. Key parameters, such as the energy spectrum, angular flux distribution, and pulse time distribution, were incorporated meticulously. Notably, the pulse time distribution was derived from the processed experimental data, as shown in Fig. 4(d), to provide a realistic representation of neutron-emission timing. Furthermore, the neutron-energy spectrum

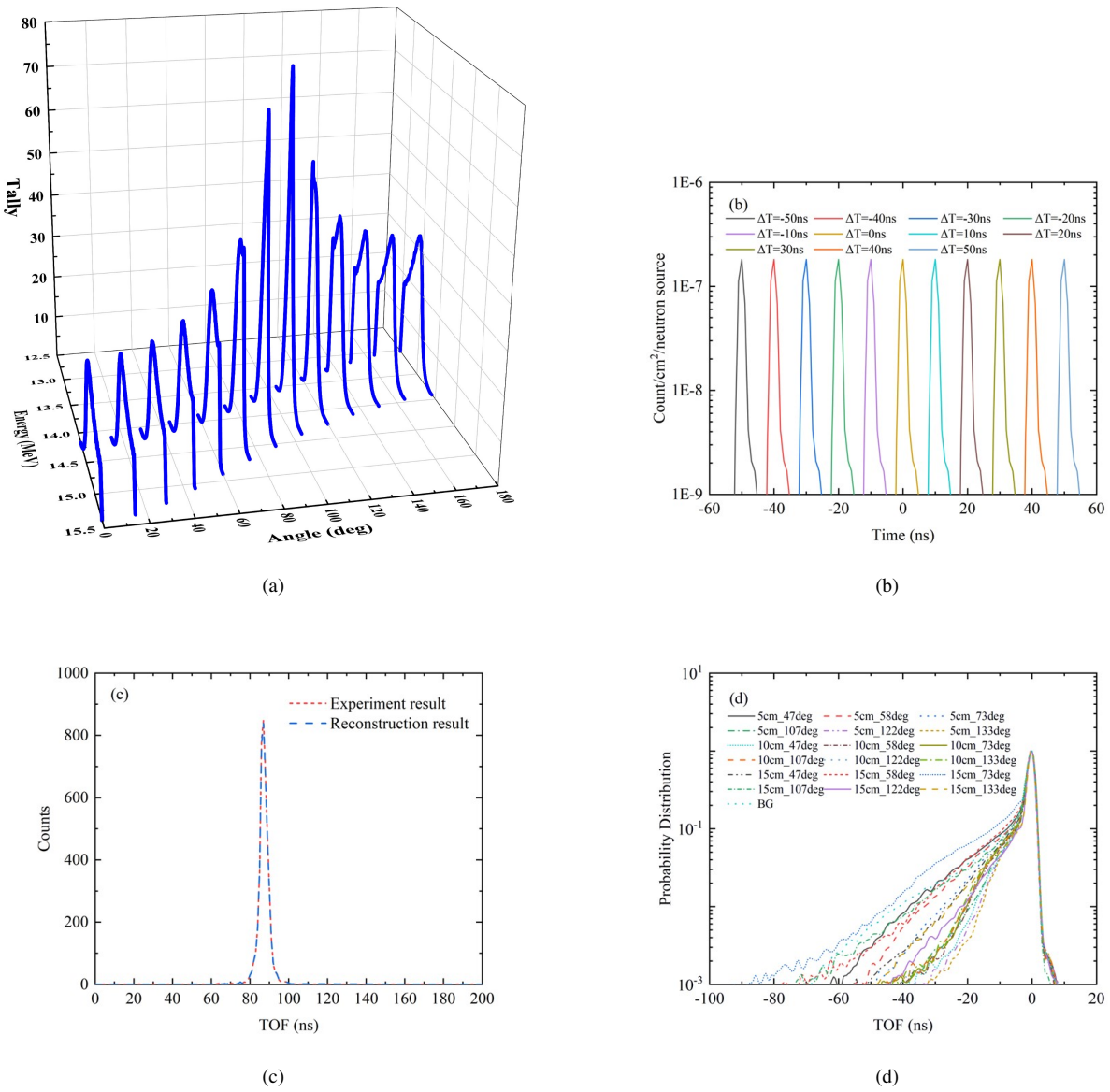

Fig. 4. (Color online) (a) Angular distribution of D–T neutrons calculated using TARGET, which provides essential input for simulation. (b) TOF spectra of neutrons generated at different times, which were recorded by the 0° monitoring detector and used for constructing the response matrix. (c) Comparison between reconstructed pulse time distribution and experimental results, which shows excellent agreement. (d) Pulse time distributions under 18 different experimental conditions for bismuth integral experiments.

and angular distribution accounted for both the D–T and D–D reactions. They were obtained by converting the count rates of alpha particles and protons observed in the accompanying particle spectrum to ensure a comprehensive and accurate source description. This integration of experimental data into simulations provides a strong foundation for analyzing neutron interactions with bismuth.

Additionally, the simulations considered the neutron-detection efficiency of the main detector, which is a critical factor that affects the accuracy of the TOF spectra. The detection efficiency was modeled based on experimental calibration data, as shown in Fig. 5. By incorporating the detector efficiency curve into the simulations, the calculated spectra were adjusted to reflect the actual neutron-detection probabilities, thereby enhancing the reliability of the results.

The complexity of the experimental platform, along with its numerous structural elements, renders it impractical to model every detail using physics-based approaches. Meanwhile, the simulation focused on neutrons traveling within a solid angle encompassing the detector and sample, thus effectively excluding neutrons scattered from walls, floors, and other components. These scattered neutrons negligibly affect the experimental results. However, critical structures, such as the target, collimator, and sample, were modeled in detail to ensure accurate neutron-transport simulations.

The simulation model was validated through a compari-

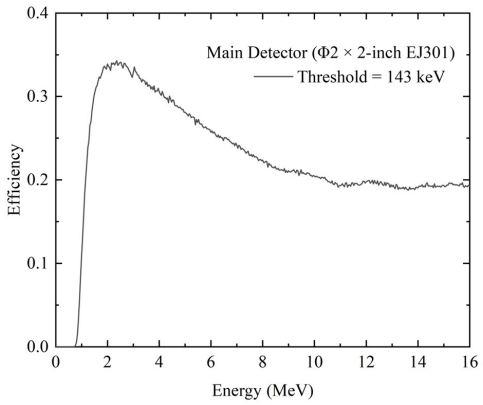

Fig. 5. Neutron-detection efficiency curve of main detector at threshold energy of 143 keV.

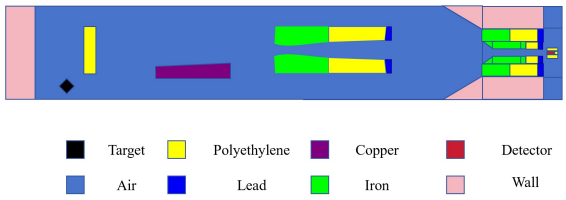

Fig. 6. (Color online) Schematic diagram of simulation model in MCNP program.

son with results obtained from standard polyethylene samples. The accuracy of the model was assessed comprehensively by comparing the simulated TOF spectra with the experimental data, particularly within the n-p scattering peak energy region. Excellent agreement between the simulated results for polyethylene and the experimental measurements confirms that the simulation model possesses the required precision and reliability.

To simplify the representation of the experimental platform, the latter was modeled as a cylindrical air-filled volume. The key components, including the target, collimator, and sample, were reconstructed with precise dimensions and structural details. The simulation was based on nuclear data from multiple sources: CENDL-3.2, ENDF/B-VIII.0, JENDL-5, and JEFF-3.3 for the sample, and ENDF/B-VIII.0 for other structural materials.

The MCNP simulations yielded TOF spectra that represented the probability of neutron detection per unit of emitted neutrons, normalized to the effective area of the main detector. This normalization allowed for a direct and meaningful comparison with the experimentally measured spectra. The comprehensive modeling approach and validation against standard samples ensured that the simulation framework was robust and suitable for analyzing neutron interactions with bismuth. The detailed setup and geometry used in the simulations (see Fig. 6) highlight the importance of modeling the critical components and conditions.

IV. RESULTS AND DISCUSSION

A. Validation with Standard Sample

To validate the reliability and accuracy of the experimental platform rigorously, a series of measurements was performed using a standard polyethylene sample measuring 30 cm × 30 cm × 5 cm. The experiments were conducted at three distinct angles: 47°, 61°, and 79°. The rationale for selecting multiple angles was to shift the n-p scattering peak across different energy regions, thereby ensuring comprehensive verification within the energy range of 0.8 to 16 MeV. This approach allowed for a comprehensive assessment of the integral experiment platform's capability in accurately evaluating the nuclear-data accuracy of materials within the relevant energy domain.

The results, as depicted in Fig. 7, reveal a high level of consistency between the measured and simulated neutron TOF spectra. Specifically, within the n-p scattering peak energy region, the C/E ratios for all four nuclear-data libraries—CENDL-3.2, ENDF/B-VIII.0, JENDL-5, and JEFF-3.3— remained within the range of 1 ± 0.03. This level of agreement is within the experimental uncertainties, thus confirming the accuracy and reliability of the experimental system. The observed consistency across different angles and energy regions demonstrates the robustness of the platform in capturing neutron transport phenomena with high precision.

B. Bismuth Results

The experimental results for bismuth are comprehensively presented in Fig. 8. Additionally, the figures shows a comparison between 18 sets of experimental data and simulation results across three sample thicknesses (5, 10, and 15 cm) and six angles (47°, 58°, 73°, 107°, 122°, and 133°). Each dataset was juxtaposed with the simulation results derived from four nuclear-data libraries: CENDL-3.2, ENDF/B-VIII.0, JENDL-5, and JEFF-3.3. Notably, significant discrepancies were observed between the different libraries, thus highlighting variations in their accuracy and reliability in modeling neutron interactions with bismuth.

To provide further insights into these differences, Fig. 9 illustrates the secondary neutron-energy spectra generated by 14.5 MeV incident neutrons interacting with bismuth, as calculated using each nuclear-data library. The original data were obtained using NDPlot [35], which is a computational tool developed by the China Nuclear Data Center for processing and visualizing nuclear data. Additionally, the figure shows the energy-spectrum distributions for various reaction channels, including elastic scattering, discrete inelastic scattering to specific energy levels, continuous inelastic scattering to a range of levels, and the (n, 2n) reaction. These spectra were segmented into energy regions based on the dominant reaction mechanisms, thus allowing for a structured assessment of the contributions from each reaction type.

Considering the various flight distances at different angles, the partition of the TOF spectra into energy regions requires

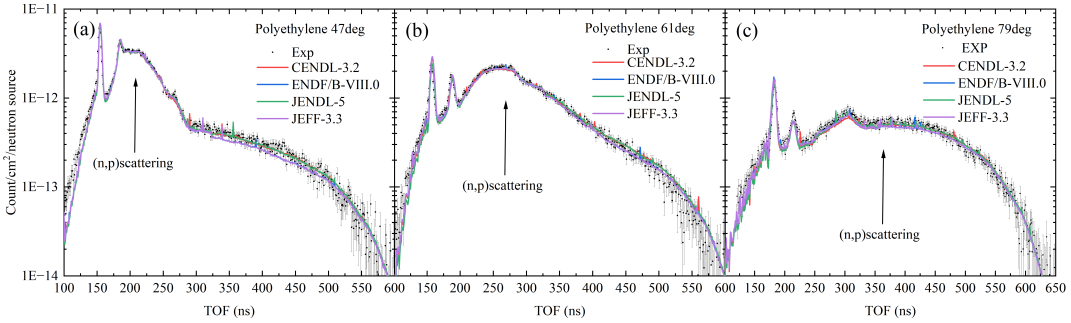

Fig. 7. (Color online) Comparison between experimental and simulated results for standard polyethylene sample at three angles: (a) 47°, (b) 61°, and (c) 79°. Excellent agreement is shown in n-p scattering peak energy region.

Table 1. Time-of-flight (TOF) spectrum ranges for different energy regions at various measurement angles.

Angle	TOF (ns)			
(deg)	(n,el)	(n,n') discrete	(n,n') continuum	(n,2n)
47	132~156	160~172	176~216	220~608
58	132~156	160~172	176~216	220~616
73	132~160	164~176	180~220	224~624
107	140~160	164~176	180~224	228~636
122	144~164	168~180	184~228	232~644
133	148~168	172~184	188~232	236~652

adjustments specific to each angle. These partitions were determined based on the secondary neutron-energy spectra shown in Fig. 9, along with the calculated flight paths for the different reaction channels. Specifically, the TOF values were derived from the sum of (1) the distance from the neutron source to the sample (neutron energy ≈ 14.5 MeV) and (2) the distance from the sample to the detector (where the neutron energy corresponds to the reaction-channel intersection points). The final TOF partitions, as summarized in Table 1, ensured an accurate interpretation of the TOF data by accounting for differences in the neutron travel paths and energy spectra. Using these energy-region partitions presented in Table 1, the C/E values for different angles, thicknesses, and energy ranges were calculated by comparing the experimental results with the corresponding theoretical calculations. The summarized values in Table 2 provide a comprehensive evaluation of nuclear-data performance across different conditions. To illustrate the variations in C/E values under the same bismuth thicknesses at different angles, Figs. 10 to 12 present the results for the four nuclear-data libraries: CENDL-3.2, ENDF/B-VIII.0, JENDL-5, and JEFF-3.3.

This systematic evaluation provides a comprehensive basis for understanding the performances of the nuclear-data libraries under various experimental conditions. The results for different bismuth thicknesses at the same angle showed a high degree of consistency, as reflected by similar trends across the measurements. This consistency validates the reliability and robustness of the experimental setup, thereby confirming the soundness of the methodology and the stability of the data acquisition.

C. Detailed Discussion on Bismuth Nuclear Data

This section provides a comprehensive analysis of the bismuth experimental data, with emphasis on the differences among the four nuclear-data libraries——CENDL-3.2, ENDF/B-VIII.0, JENDL-5, and JEFF-3.3——across various reaction channels and angles. The evaluation was based on a comparison of the C/E values to assess the accuracy and reliability of each library. Figure 13, which was created using NDPlot, presents the angular distributions and energy spectra of secondary neutrons generated by 14.5 MeV incident neutrons interacting with bismuth for different reaction channels, thus facilitating in the detailed analysis. The C/E values of all three sample thicknesses (5, 10, and 15 cm) were considered. Although the absolute values varied slightly with the thickness, the overall angular dependence remained consistent. Therefore, our discussion focuses on the general trend observed across all thicknesses instead of specific values for a single sample.

(1) **Elastic Energy Region**: Fig. 13(a) depicts the angular distribution of elastic scattering as predicted by the four nuclear-data libraries: CENDL-3.2, ENDF/B-VIII.0, JENDL-5, and JEFF-3.3. The overall trend indicates that the discrepancies among the libraries became more pronounced at larger angles. The C/E values revealed minimal deviations at smaller angles, specifically 47° and 58°, although ENDF/B-VIII.0 exhibited a slight overestimation at 58° compared with the other libraries. However, at 73°, the JEFF-3.3 library exhibited a higher C/E value than the other libraries. At 107°, all four libraries clearly indicated overestimations, with elevated C/E values across the board. At 122°, only the CENDL-3.2 library maintained a consistent C/E value without overestimation, whereas the other libraries showed a clear upward deviation, as shown in Fig. 13(a). The divergence of the ENDF/B-VIII.0, JENDL-5, and JEFF-3.3 libraries at this angle highlights the differences in their modeling of neutron interactions. At 133°, both ENDF/B-VIII.0 and JEFF-3.3 indicated higher C/E values. This observation contrasts slightly with the trends shown in Fig. 13(a), primar-

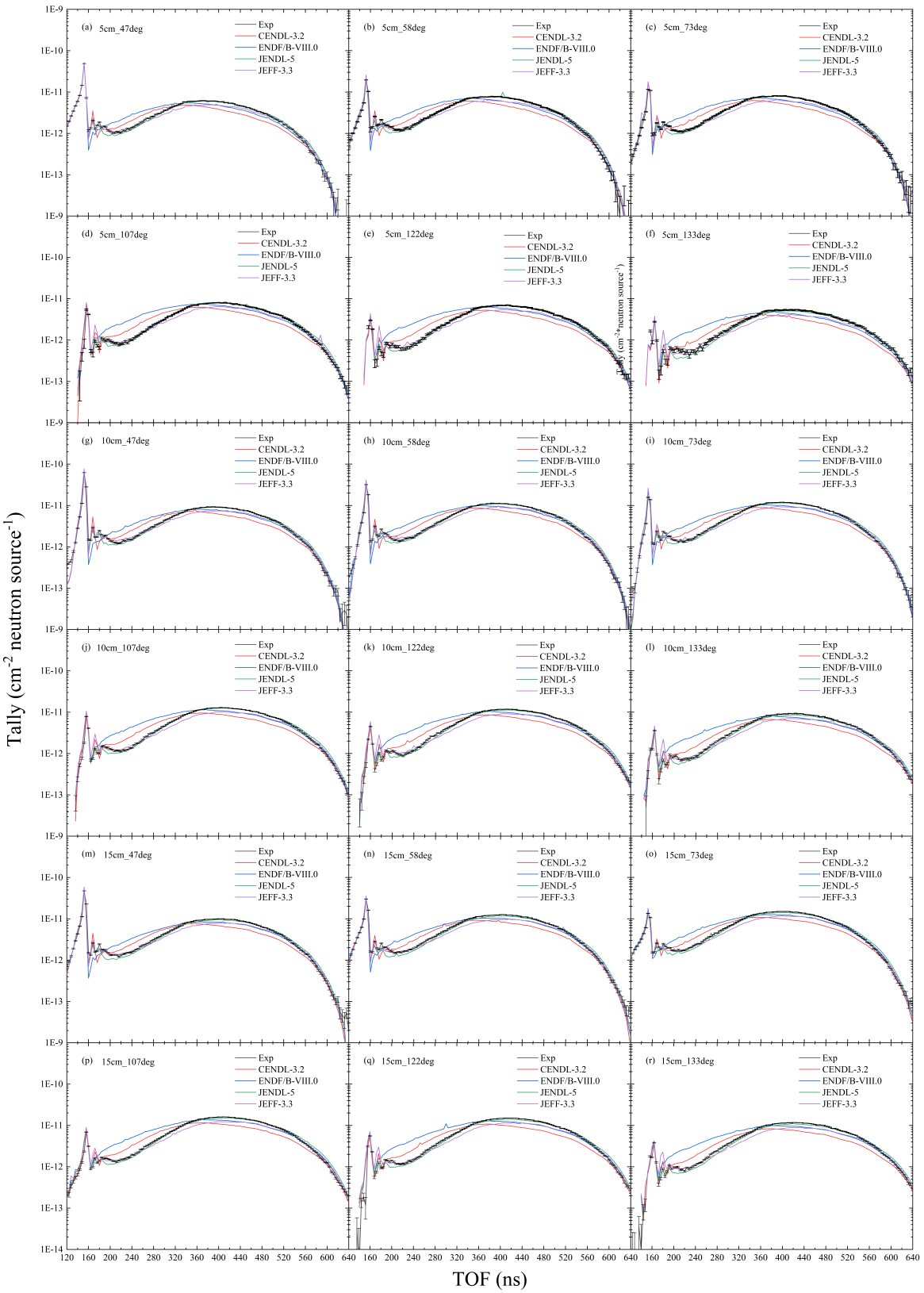

Fig. 8. (Color online) Comparison of experimental results with simulations from four different nuclear-data libraries—CENDL—3.2, ENDF/B-VIII.0, JENDL-5, and JEFF-3.3——across 18 different conditions.

Table 2. C/E values for various thicknesses, measurement angles, reaction channels, and nuclear-data libraries.

Sample (cm)	Angle (deg)	Reaction	CENDL-3.2	ENDF/B-VIII.0	JENDL-5	JEFF-3.3
5	47	(n,el)	1.011 ± 0.032	1.062 ± 0.034	1.039 ± 0.033	1.075 ± 0.034
		(n,n') discrete	1.193 ± 0.038	0.517 ± 0.017	0.905 ± 0.029	0.960 ± 0.031
		(n,n') continuum	0.953 ± 0.031	1.244 ± 0.040	0.817 ± 0.030	0.953 ± 0.031
		(n,2n)	0.828 ± 0.027	0.994 ± 0.032	0.991 ± 0.032	0.859 ± 0.028
	58	(n,el)	1.050 ± 0.034	1.117 ± 0.036	1.020 ± 0.033	1.082 ± 0.035
		(n,n') discrete	1.239 ± 0.040	0.637 ± 0.020	0.910 ± 0.029	1.078 ± 0.035
		(n,n') continuum	0.942 ± 0.030	1.304 ± 0.042	0.787 ± 0.025	0.896 ± 0.029
		(n,2n)	0.824 ± 0.026	1.008 ± 0.032	1.003 ± 0.032	0.849 ± 0.027
	73	(n,el)	1.105 ± 0.035	1.176 ± 0.038	1.139 ± 0.036	1.237 ± 0.040
		(n,n') discrete	1.146 ± 0.037	0.816 ± 0.026	0.989 ± 0.032	1.190 ± 0.038
		(n,n') continuum	1.088 ± 0.035	1.593 ± 0.051	0.800 ± 0.026	0.919 ± 0.029
		(n,2n)	0.818 ± 0.026	0.962 ± 0.031	0.993 ± 0.032	0.829 ± 0.027
	107	(n,el)	1.150 ± 0.037	1.369 ± 0.044	1.385 ± 0.044	1.409 ± 0.045
		(n,n') discrete	1.438 ± 0.046	1.256 ± 0.040	1.144 ± 0.037	1.981 ± 0.063
		(n,n') continuum	1.308 ± 0.042	2.241 ± 0.072	0.893 ± 0.029	1.000 ± 0.032
		(n,2n)	0.849 ± 0.027	1.075 ± 0.034	1.032 ± 0.033	0.851 ± 0.027
	122	(n,el)	0.966 ± 0.031	1.236 ± 0.040	1.120 ± 0.036	1.225 ± 0.039
		(n,n') discrete	1.522 ± 0.049	1.605 ± 0.051	1.273 ± 0.041	2.703 ± 0.086
		(n,n') continuum	1.385 ± 0.044	2.499 ± 0.080	0.876 ± 0.028	1.059 ± 0.034
		(n,2n)	0.818 ± 0.026	1.047 ± 0.034	0.988 ± 0.032	0.827 ± 0.026
	133	(n,el)	1.011 ± 0.032	1.151 ± 0.037	1.069 ± 0.034	1.136 ± 0.036
		(n,n') discrete	1.425 ± 0.046	1.622 ± 0.052	1.121 ± 0.036	2.870 ± 0.092
		(n,n') continuum	1.220 ± 0.039	2.361 ± 0.076	0.759 ± 0.024	0.911 ± 0.029
		(n,2n)	0.775 ± 0.025	0.998 ± 0.032	0.934 ± 0.030	0.791 ± 0.025
10	47	(n,el)	1.018 ± 0.033	1.080 ± 0.035	1.048 ± 0.034	1.079 ± 0.035
		(n,n') discrete	1.267 ± 0.041	0.461 ± 0.015	0.878 ± 0.028	0.944 ± 0.030
		(n,n') continuum	0.935 ± 0.030	1.192 ± 0.038	0.846 ± 0.027	0.981 ± 0.031
		(n,2n)	0.845 ± 0.027	1.016 ± 0.033	0.996 ± 0.032	0.865 ± 0.028
	58	(n,el)	1.060 ± 0.034	1.113 ± 0.036	1.045 ± 0.033	1.077 ± 0.034
		(n,n') discrete	1.145 ± 0.037	0.472 ± 0.015	0.845 ± 0.027	0.972 ± 0.031
		(n,n') continuum	0.962 ± 0.031	1.302 ± 0.042	0.835 ± 0.027	0.980 ± 0.031
		(n,2n)	0.843 ± 0.027	1.024 ± 0.033	1.003 ± 0.032	0.862 ± 0.028
	73	(n,el)	1.074 ± 0.034	1.140 ± 0.036	1.079 ± 0.035	1.224 ± 0.039
		(n,n') discrete	1.170 ± 0.037	0.725 ± 0.023	0.993 ± 0.032	1.243 ± 0.040
		(n,n') continuum	1.088 ± 0.035	1.522 ± 0.049	0.833 ± 0.027	0.952 ± 0.030
		(n,2n)	0.822 ± 0.026	0.953 ± 0.031	0.988 ± 0.032	0.835 ± 0.027
	107	(n,el)	1.151 ± 0.037	1.333 ± 0.043	1.341 ± 0.043	1.379 ± 0.044
		(n,n') discrete	1.408 ± 0.045	1.192 ± 0.038	1.129 ± 0.036	1.884 ± 0.060
		(n,n') continuum	1.269 ± 0.041	2.121 ± 0.068	0.873 ± 0.028	0.983 ± 0.031
		(n,2n)	0.819 ± 0.026	1.040 ± 0.033	0.999 ± 0.032	0.831 ± 0.027
	122	(n,el)	0.989 ± 0.032	1.320 ± 0.042	1.185 ± 0.038	1.305 ± 0.042
		(n,n') discrete	1.500 ± 0.048	1.585 ± 0.051	1.219 ± 0.039	2.454 ± 0.079
		(n,n') continuum	1.379 ± 0.044	2.452 ± 0.079	0.890 ± 0.029	1.048 ± 0.034
		(n,2n)	0.799 ± 0.026	1.026 ± 0.033	0.975 ± 0.031	0.817 ± 0.026
	133	(n,el)	1.063 ± 0.034	1.260 ± 0.040	1.143 ± 0.037	1.286 ± 0.041
		(n,n') discrete	1.483 ± 0.047	1.851 ± 0.059	1.187 ± 0.038	2.729 ± 0.087
		(n,n') continuum	1.300 ± 0.042	2.512 ± 0.080	0.835 ± 0.027	0.992 ± 0.032
		(n,2n)	0.782 ± 0.025	1.005 ± 0.032	0.946 ± 0.030	0.806 ± 0.026
15	47	(n,el)	0.996 ± 0.032	1.047 ± 0.034	1.020 ± 0.033	1.032 ± 0.033
		(n,n') discrete	1.228 ± 0.039	0.449 ± 0.014	0.849 ± 0.027	0.952 ± 0.030
		(n,n') continuum	0.931 ± 0.030	1.186 ± 0.038	0.801 ± 0.026	0.963 ± 0.031
		(n,2n)	0.835 ± 0.027	0.992 ± 0.032	0.965 ± 0.031	0.843 ± 0.027
	58	(n,el)	0.982 ± 0.031	1.017 ± 0.033	0.979 ± 0.031	1.004 ± 0.032
		(n,n') discrete	1.109 ± 0.036	0.539 ± 0.017	0.820 ± 0.026	0.938 ± 0.030
		(n,n') continuum	0.966 ± 0.031	1.320 ± 0.042	0.793 ± 0.025	0.917 ± 0.029
		(n,2n)	0.818 ± 0.026	0.979 ± 0.031	0.953 ± 0.031	0.825 ± 0.026
	73	(n,el)	1.019 ± 0.033	1.072 ± 0.034	1.006 ± 0.032	1.055 ± 0.034
		(n,n') discrete	1.067 ± 0.034	0.807 ± 0.026	0.904 ± 0.029	1.059 ± 0.034
		(n,n') continuum	1.142 ± 0.037	1.626 ± 0.052	0.817 ± 0.026	0.939 ± 0.030
		(n,2n)	0.808 ± 0.026	0.989 ± 0.032	0.968 ± 0.031	0.825 ± 0.026
	107	(n,el)	1.143 ± 0.037	1.326 ± 0.042	1.274 ± 0.041	1.355 ± 0.043
		(n,n') discrete	1.314 ± 0.042	1.204 ± 0.039	1.036 ± 0.033	1.642 ± 0.053
		(n,n') continuum	1.285 ± 0.041	2.101 ± 0.067	0.862 ± 0.028	0.983 ± 0.031
		(n,2n)	0.812 ± 0.026	1.021 ± 0.033	0.985 ± 0.032	0.828 ± 0.027
	122	(n,el)	1.023 ± 0.033	1.349 ± 0.043	1.219 ± 0.039	1.314 ± 0.042
		(n,n') discrete	1.398 ± 0.045	1.453 ± 0.047	1.124 ± 0.036	2.158 ± 0.069
		(n,n') continuum	1.325 ± 0.042	2.346 ± 0.075	0.864 ± 0.028	1.003 ± 0.032
		(n,2n)	0.793 ± 0.025	1.013 ± 0.032	0.963 ± 0.031	0.812 ± 0.026
	133	(n,el)	1.067 ± 0.034	1.236 ± 0.040	1.156 ± 0.037	1.225 ± 0.039
		(n,n') discrete	1.375 ± 0.044	1.670 ± 0.053	1.114 ± 0.036	2.478 ± 0.079
		(n,n') continuum	1.341 ± 0.043	2.538 ± 0.081	0.853 ± 0.027	1.040 ± 0.033
		(n,2n)	0.777 ± 0.025	0.997 ± 0.032	0.942 ± 0.030	0.801 ± 0.026

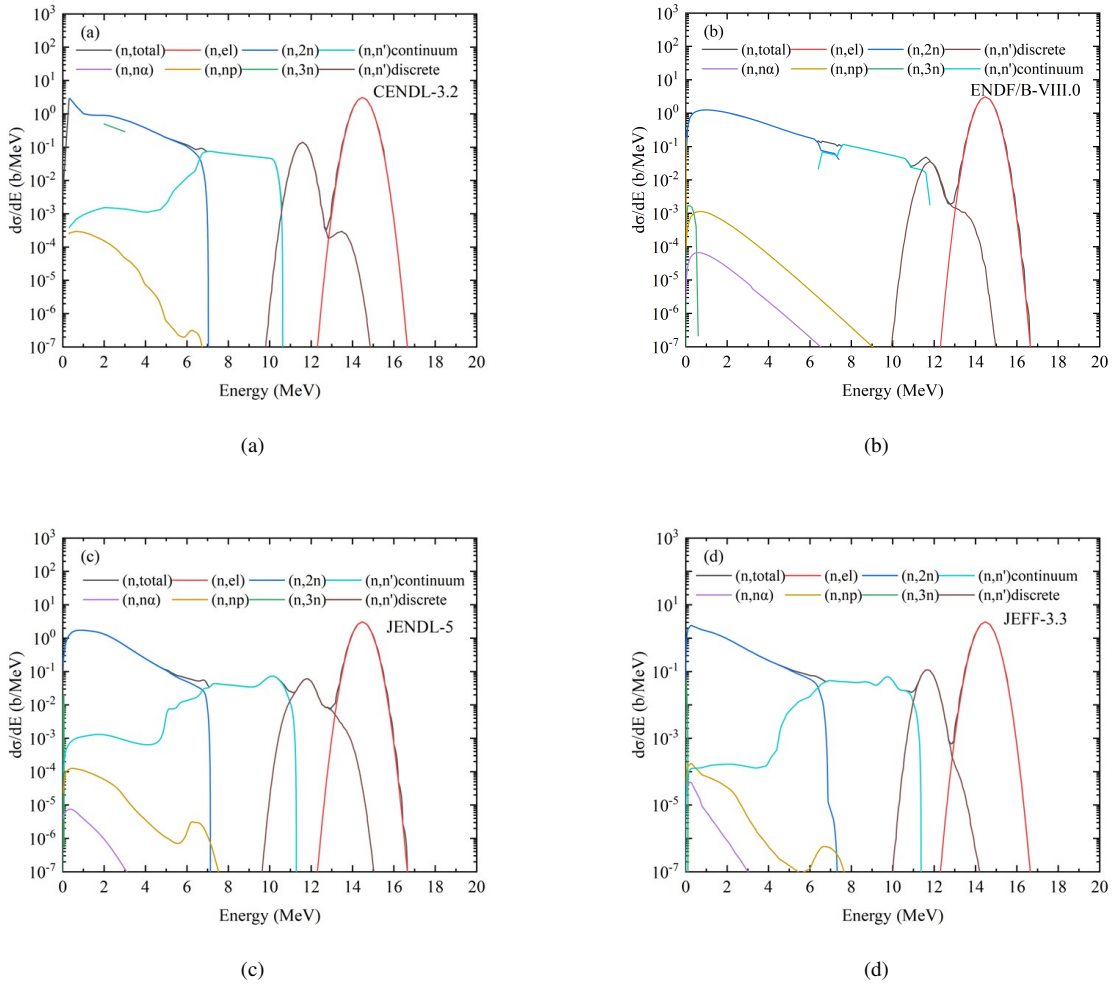

Fig. 9. (Color online) Secondary neutron-energy spectra yielded by 14.5 MeV neutrons incident on bismuth, as generated by four different nuclear-data libraries: (a) CENDL-3.2, (b) ENDF/B-VIII.0, (c) JENDL-5, and (d) JEFF-3.3. The spectra are segmented into different reaction channels for detailed analysis.

ily because of the effect of discrete inelastic scattering on the separated energy levels. At large angles, the contribution of elastic scattering decreased, whereas that of discrete inelastic scattering became more significant. Figure 9 shows that JEFF-3.3 exerted the least prominent effect of discrete inelastic scattering on elastic scattering (with minimal energy overlap), followed by CENDL-3.2, whereas ENDF/B-VIII.0, and JENDL-5 exhibited considerably more prominent effects. However, Fig. 13(b) reveals that JEFF-3.3 significantly overestimated discrete inelastic scattering in absolute magnitude, thus resulting in elevated C/E values in the elastic scattering energy region at large angles despite its reduced effect on elastic scattering. By contrast, CENDL-3.2 not only exhibited a less prominent effect by discrete inelastic scattering but also has a lower discrete inelastic scattering cross-section overlapping with the elastic scattering region. Consequently, at 133°, CENDL-3.2 performed the best in terms of C/E values within this elastic scattering energy region.

(2) **Discrete Inelastic Scattering**: Fig. 13(b) illustrates the significant differences among the four nuclear-data libraries in predicting discrete inelastic scattering for bismuth. These discrepancies became increasingly evident at various angles, thus emphasizing the variability in the manner by which each library models neutron interactions. The C/E values offer further insights into these differences. At smaller angles, specifically 47° and 58°, the JEFF-3.3 library demonstrated the closest agreement with the measured data. Conversely, at larger angles, i.e., 73°, 107°, and 133°, JENDL-5 showed better correspondence. Nonetheless, a significant overestimation occurred at 122° across all libraries, thus indicating a common challenge in accurately modeling neutron interactions at this angle. The CENDL-3.2 library consistently overestimated across the entire energy region but maintained a relatively reasonable angular-distribution pattern. Meanwhile, ENDF/B-VIII.0 exhibited insufficient detailed angular-distribution data for discrete inelastic scattering, thus resulting in substantial

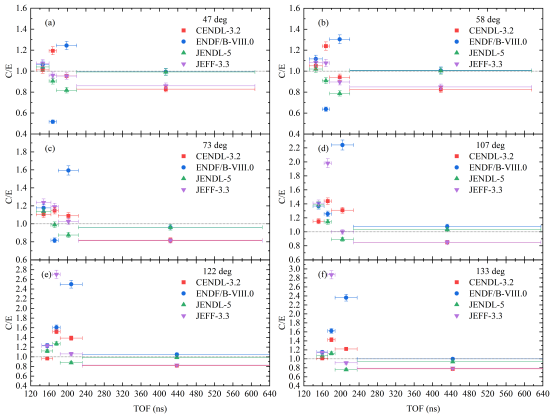

Fig. 10. (Color online) C/E values for 5 cm bismuth sample under different nuclear-data libraries, plotted as a function of energy region at various angles.

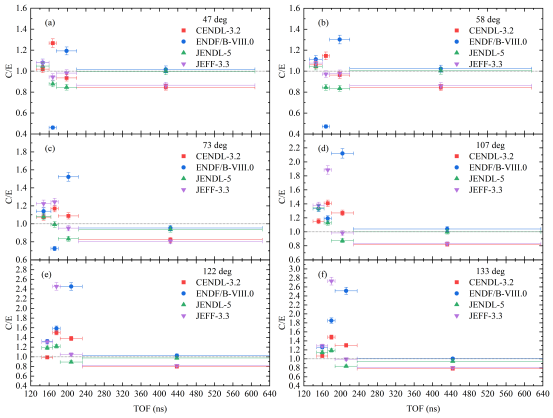

Fig. 11. (Color online) C/E values for 10 cm bismuth sample under different nuclear-data libraries, plotted as a function of energy region at various angles.

underestimations at smaller angles, which diminished with increasing angle. JENDL-5 generally aligned well at larger angles but underestimated in the discrete inelastic scattering region at smaller angles, likely owing to the broader energy range for discrete inelastic scattering that overlapped with the elastic scattering energy region, as depicted in Fig.9(c). During energy segmentation, the elastic scattering region contributed partly to the discrete inelastic scattering, thus resulting lower C/E values in the discrete inelastic scattering region. At 47°, the elastic scattering cross-section of JENDL-5 was slightly larger than that of JEFF, as shown in Fig.13(b), whereas the C/E value of JENDL-5 was lower, thus reflecting the overlap effect. The JEFF-3.3 library performed well at

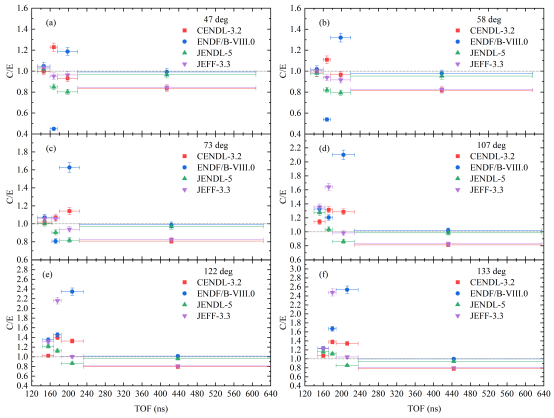

Fig. 12. (Color online) C/E values for 15 cm bismuth sample under different nuclear-data libraries, plotted as a function of energy region at various angles.

smaller angles but overestimated at larger angles. This trend highlights the limitations in the modeling of angular distributions for discrete inelastic scattering within the JEFF-3.3 dataset.

(3) **Continuous Inelastic Scattering**: The angular distributions of continuous inelastic scattering, as predicted by the four nuclear-data libraries, revealed substantial differences, as shown in Fig.13(c). The C/E values indicated that at 47°, the CENDL-3.2 and JEFF-3.3 libraries yielded the most accurate results, whereas JENDL-5 underestimated and ENDF/B-VIII.0 overestimated. At 58°, the CENDL-3.2 library showed a slightly better agreement than JEFF-3.3, whereas ENDF/B-VIII.0 exhibited a severe overestimation and JENDL-5 continued to underestimate. At 73°, CENDL-3.2 showed a slight overestimation and JEFF-3.3 showed a slight underestimation; however, both libraries presented comparable deviations. By contrast, the remaining two libraries—ENDF/B-VIII.0 and JENDL-5—continued to exhibit significant discrepancies.

At larger angles (107°, 122°, and 133°), the JEFF-3.3 library demonstrated the best overall agreement with the experimental data. Figure 13(c) shows that the angular distributions of CENDL-3.2 and JEFF-3.3 intersected near 50°, where they almost coincided. Beyond this point, JEFF-3.3's downward trend was steeper, thus resulting in lower values compared with the case of CENDL-3.2 at larger angles. The analysis of deviations indicates that at 58°, the data of JEFF-3.3 aligned more closely with those of CENDL-3.2, whereas at 73°, although one library slightly overestimated and the other slightly underestimated, the magnitudes of their deviations were comparable. As the angle increased further, the predictions of JEFF-3.3 aligned more accurately with the experimental results.

The ENDF/B-VIII.0 library continued to exhibit insufficient detailed angular-distribution information, thus resulting

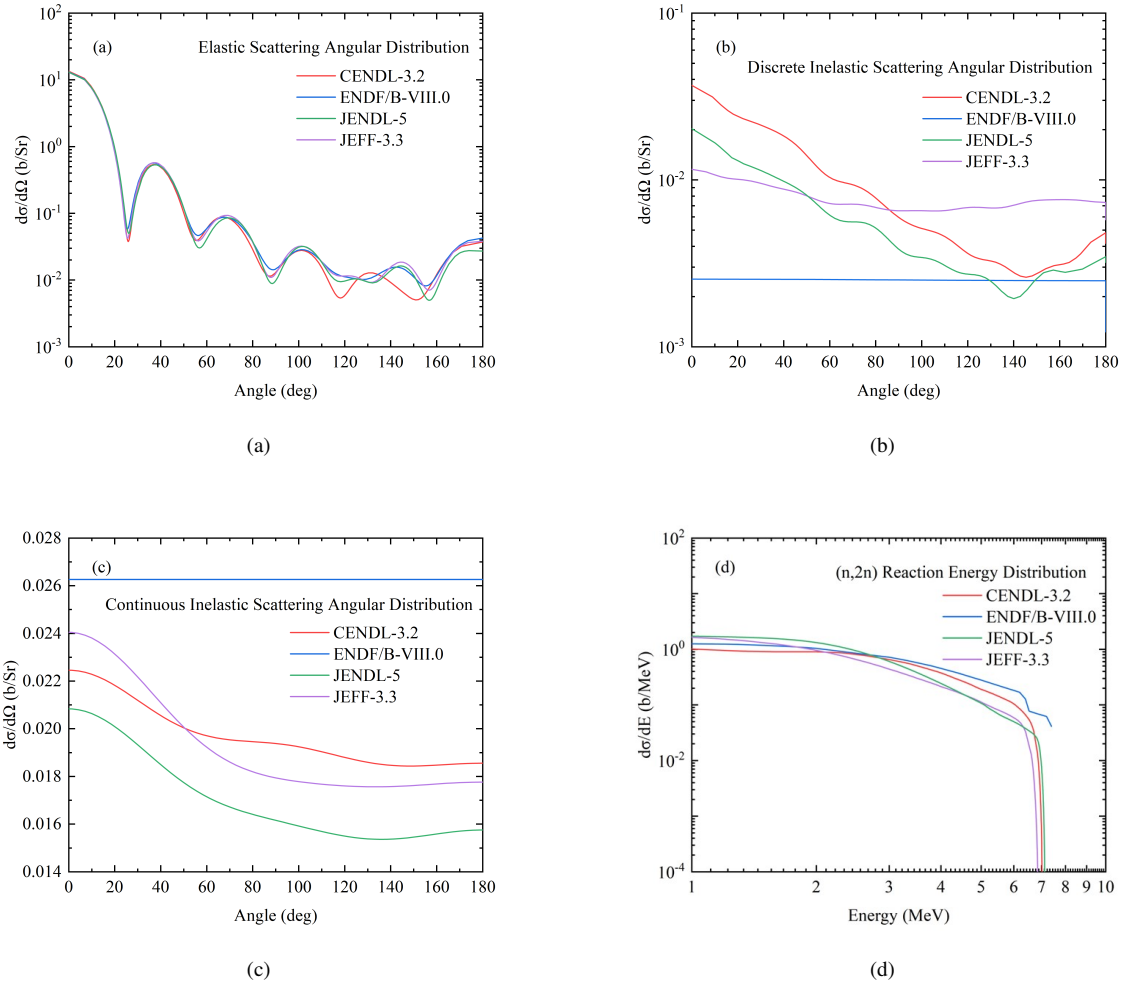

Fig. 13. (Color online) Angular distributions and energy spectra of secondary neutrons for different reaction channels: (a) elastic scattering angular distribution, (b) discrete inelastic scattering angular distribution, (c) continuous inelastic scattering angular distribution, and (d) secondary energy spectrum distribution for (n, 2n) reaction.

in a consistent and significant overestimation. Considering the overall downward trend in the angular distribution, the magnitude of this overestimation became more pronounced at larger angles. However, the JENDL-5 library consistently underestimated across all angles, although it maintained a trend similar to that of the experimental data.

(4) **(n, 2n) Reaction**: Because the (n, 2n) reaction is a multibody process, its angular distribution typically exhibits minimal variations. Therefore, Fig. 13(d) focuses on the distribution of the secondary neutron-energy spectra. The C/E values indicate that ENDF/B-VIII.0 demonstrated the best overall agreement, followed closely by JENDL-5. By contrast, both CENDL-3.2 and JEFF-3.3 exhibited underestimations, which is consistent with the trend observed in the integrated energy spectrum values.

Whereas ENDF/B-VIII.0 indicated the closest agreement in terms of C/E values, JENDL-5 showed greater overall consistency with the experimental data. This discrepancy arises because ENDF/B-VIII.0 tends to overestimate in the higher energy range (3–7 MeV) and underestimate in the lower energy range (< 3 MeV), as shown in Fig. 13(d). This variation was particularly pronounced when the experimental and simulated data were compared, as shown in Fig. 8, thus highlighting the differences between the high- and low-energy overestimations.

Based on a comprehensive analysis of each energy region and angle , we recommend the following for selecting the most suitable nuclear-data library: For the **elastic energy region**, CENDL-3.2 provided the best overall agreement with the experimental data across all angles. In the **discrete inelastic scattering region**, JENDL-5 provided the best agreement at larger angles. At smaller angles, JEFF-3.3 performed well overall, while CENDL-3.2 demonstrated reasonable agreement in some cases. For the **continuous inelastic scattering region**, JEFF-3.3 provided the best overall agreement, particularly at large angles, whereas CENDL-3.2 performed well at

58°. Finally, in the **(n, 2n) energy region**, ENDF/B-VIII.0 delivered the most similar C/E values, thus rendering it the best option for a high overall agreement; however, JENDL-5 is recommended when consistency across the full energy region is prioritized.

V. CONCLUSION

This study performed a comprehensive benchmark analysis of neutron interactions with bismuth using experimental data obtained at various angles and sample thicknesses. The experiments provided high-quality TOF spectra, which were then compared with simulation results generated using four nuclear-data libraries: CENDL-3.2, ENDF/B-VIII.0, JENDL-5, and JEFF-3.3. The experimental setup, which was designed to enable high-precision measurements, enabled a detailed assessment of neutron behavior, whereas the simulations offered insights into the performance of each nuclear-data library.

The experiments included measurements using a standard polyethylene sample at three different angles to validate the reliability of the results across the entire energy range. Additionally, neutron-leakage spectra were measured for bismuth samples at three thicknesses and six angles, thus resulting in 18 datasets. In processing the experimental data, the pulse time distribution was reconstructed using the MLEM algorithm in conjunction with the neutron TOF spectra from the monitoring detectors. The D–T/D–D reaction ratio was determined using a SiC-associated particle detector, which effectively distinguished alpha particles from the D–T reaction and protons from the D–D reaction by separately recording their count rates. The processing of experimental data, including the pulse time distribution and mixed field analysis, provided a comprehensive understanding of the neutron-source characteristics, thereby establishing a solid foundation for the simulation.

The simulation incorporated an experimentally derived pulse time distribution and accounted for the mixed D–T/D–D neutron field. The reliability of the simulation model was validated using the standard polyethylene sample, where all four nuclear-data libraries yielded C/E values of 1 ± 0.03, thus confirming that the entire experimental–simulation setup satisfied the requirements for integral experiments. Analysis of the 18 experimental scenarios resulted in the following conclusions:

The key findings showed that for the **elastic scattering region**, CENDL-3.2, provided the most reliable results across all angles. In the **discrete inelastic scattering region**, JEFF-3.3 demonstrated better agreement at small angles, whereas JENDL-5 demonstrated higher accuracy at larger angles. The **continuous inelastic scattering region** indicated that JEFF-3.3 provided the best overall agreement across all angles, whereas CENDL-3.2 performed well at 58°. While ENDF/B-VIII.0 exhibited the closest overall agreement in the **(n, 2n) reaction region**, JENDL-5 provided more consistent results across the energy region.

DATA AVAILABILITY

The dataset supporting this study, including 19 sets of neutron TOF leakage spectra——18 sets for bismuth samples under different experimental conditions and 1 set for background measurements——along with the simulation models used in this study, has been deposited in the *Science Data Bank* (ScienceDB). The dataset is available under the *Nuclear Science and Technology (NST)* collection and can be accessed via the DOI: https://doi.org/10.57760/sciencedb.j00186.00533. Researchers interested in using the data are required to submit an application through ScienceDB. Upon approval, access will be granted according to the repository guidelines.

VI. ACKNOWLEDGMENTS

The authors would like to thank the Cockcroft–Walton accelerator group for their excellent operation of the D–T neutron source in the CIAE.

[1] Y.C. Wu, Y.Q. Bai, S. Yong et al., Development strategy and conceptual design of China Lead-based Research Reactor. Ann. Nuc. Ene. **87**, 511–516 (2016).doi:10.1016/j.anucene.2015.08.015

[2] S.S. Kapoor, Accelerator-driven sub-critical reactor system (ADS) for nuclear energy generation. Pramana – J. Phys. **59**, 941–950 (2002). doi:10.1007/s12043-002-0143-z

[3] P.A. Gokhale, S. Deokattey, V. Kumar et al., Accelerator driven systems (ADS) for energy production and waste transmutation: international trends in R&D. Prog. Nucl. Energy **48**, 91–102 (2006). doi:10.1016/j.pnucene.2005.09.006

[4] S.P. Simakov, V.S. Ivashkin, M.M. Korovin et al., 14 MeV Facility and Research in IPPE. Report INDC(CCP)-351, IAEA (1993).https://www.osti.gov/etdeweb/biblio/20181081

[5] Y. Oyama,S. Yamaguchi, H. Maekawa, Experimental Results of Angular Neutron Flux Spectra Leaking From Slabs of Fusion Reactor Candidate Materials (I). JAERI-M90-092 (1990). https://jopss.jaea.go.jp/pdfdata/JAERI-M-90-092.pdf

[6] H. Maekawa, Y. Oyama, Experiment on angular neutron flux spectra from lead slabs bombarded by D-T neutrons. Fusion Eng. Des. **18**, 287 (1991). doi:10.1016/0920-3796(91)90140-L

[7] S. Kwon, M. Ohta, S. Sato et al., Lead benchmark experiment with DT neutrons at JAEA/FNS. Fusion Sci. Technol. **72**, 362–367 (2017). doi:10.1080/15361055.2017.1330622

[8] K. Ochiai, K. Kondo, S. Ohnishi et al., DT neutronics benchmark experiment on lead at JAEA-FNS. J. Korean Phys. Soc. **59**, 1953–1956 (2011). doi:10.3938/jkps.59.1953

[9] S.P. Simakov, A.A. Androsenko, P.A. Androsenko et al., Neutron leakage spectra from Be, Al, Fe, Ni, Pb, LiPb, Bi, U and Th sphere with T(d,n) and Cf neutron source. Fusion Technol. **1993**, 1489–1493 (1992). doi:10.1016/B978-0-444-89995-8.50292-7

[10] Z.G. Ge, R.R. Xu, H.C. Wu et al., CENDL-3.2: The new version of Chinese general purpose evaluated nuclear data library. EPJ Web Conf. **239**, 09001 (2020). doi:10.1051/epjconf/202023909001
[11] D.A. Brown, M.B. Chadwick, R. Capote et al., ENDF/B-VIII.0: The 8th Major Release of the Nuclear Reaction Data Library with CIELO-project Cross Sections, New Standards and Thermal Scattering Data. Nucl. Data Sheets **148**, 1–142 (2018). doi:10.1016/j.nds.2018.02.001
[12] O. Iwamoto, N. Iwamoto, S. Keuieda et al., Japanese evaluated nuclear data library version 5: JENDL-5. J. Nucl. Sci. Technol. **60**, 1–60 (2023). doi:10.1080/00223131.2022.2141903
[13] O. Cabellos, F. Alvarez-Velarde, M. Angelone et al., Benchmarking and validation activities within JEFF project. EPJ Web Conf. **146**, 06004 (2017). doi:10.1051/epjconf/201714606004
[14] Q. Zhao, Y.-B. Nie, Y.-Y. Ding et al., Measurement and simulation of the leakage neutron spectra from Fe spheres bombarded with 14 MeV neutrons. Nucl. Sci. Tech. **34**, 182 (2023). doi:10.1007/s41365-023-01329-6
[15] Y.-Y. Ding, Y.-B. Nie, Y. Zhang et al., Benchmark experiment on slab 238-U with D-T neutrons for validation of evaluated nuclear data. Nucl. Sci. Tech. **35**, 29 (2024). doi:10.1007/s41365-024-01386-5
[16] Z.K. Lin, Y.-B. Nie, X.Z. Cai et al., Benchmarking of ^{232}Th evaluation by a 14.8 MeV neutron leakage spectra experiment with slab samples. Ann. Nucl. Energy **96**, 181–186 (2016). doi:10.1016/j.anucene.2016.05.019
[17] F. Luo, R. Han, Z.Q. Chen, Measurement of leakage neutron spectra from graphite cylinders irradiated with D-T neutrons for validation of evaluated nuclear data. Appl. Radiat. Isot. **116**, 185–189 (2016). doi:10.1016/j.apradiso.2016.08.009
[18] S. Zhang, Z.Q. Chen, Y.-B. Nie et al., Measurement of leakage neutron spectra for Tungsten with D-T neutrons and validation of evaluated nuclear data. Fusion Eng. Des. **92**, 41–45 (2015). doi:10.1016/j.fusengdes.2015.01.010
[19] Y.-Y. Ding, Y.-B. Nie, J. Ren et al., Benchmark experiment for bismuth by slab samples with D-T neutron source. Fusion Eng. Des. **167**, 112312 (2021). doi:10.1016/j.fusengdes.2021.112312
[20] Q. Sun, Z.Q. Chen, R. Han et al., Experiment on uranium slabs of different thicknesses with D-T neutrons and validation of evaluated nuclear data. Fusion Eng. Des. **125**, 9–17 (2017). doi:10.1016/j.fusengdes.2017.10.021
[21] Y.-B. Nie, J. Ren, X.C. Ruan et al., Benchmarking of evaluated nuclear data for iron by a TOF experiment with slab samples. Fusion Eng. Des. **145**, 40–45 (2019). doi:10.1016/j.fusengdes.2019.05.021
[22] S. Zhang, Y.-B. Nie, J. Ren et al., Benchmarking of JEFF-3.2, FENDL-3.0 and TENDL-2014 evaluated data for tungsten with 14.8 MeV neutrons. Nucl. Sci. Tech. **28**, 27 (2017). doi:10.1007/s41365-017-0192-0
[23] Y.-Y. Ding, Y.-B. Nie, J. Ren et al., The benchmark experiment on slab iron with D-T neutrons for validation of evaluated nuclear data. Ann. Nucl. Energy **132**, 236–242 (2019). doi:10.1016/j.anucene.2019.04.041
[24] J. Briesmeister (Ed.), MCNP – a general Monte Carlo N-Particle transport code system, Version 4C. Report LA-13709-M (2000).https://mcnp.lanl.gov/pdf_files/TechReport_2000_LANL_LA-13709-M_Briesmeisterothers.pdf
[25] G.R. Shen, H.-T. Chen, X.-L. Guan, CIAE 600 kV ns pulse neutron generator. CERN Document Server (2001). https://cds.cern.ch/record/748219
[26] N. Evans, I.R. Brearley, M.C. Scott, Neutron yield calibration of a miniature (D-T) target assembly with associated particle monitoring. Nucl. Instrum. Methods **160**, 465–470 (1979). doi:10.1016/0029-554X(79)90202-7
[27] L. Rong, L.-B. Lin, D.-L. Wang, Measurement and check of fusion neutron yield with the method of associated particles at a large angle. Nucl. Electron. Detect. Technol. **19**, 428–432 (1999). doi:10.3969/j.issn.0258-0934.1999.06.006
[28] H.-Y. Wu, Z.-H. Li, H. Tan et al., A general-purpose digital data acquisition system (GDDAQ) at Peking University. Nucl. Instrum. Methods Phys. Res. A **975**, 164200 (2020). doi:10.1016/j.nima.2020.164200
[29] S. Guo, X.-H. Zhou, C.-M. Petrache et al., Probing the nature of the conjectured low-spin wobbling bands in atomic nuclei. Phys. Lett. B **828**, 137010 (2022). doi:10.1016/j.physletb.2022.137010
[30] D.-W. Luo, H.-Y. Wu, Z.-H. Li et al., Performance of digital data acquisition system in gamma-ray spectroscopy. Nucl. Sci. Tech. **32**, 79 (2021). doi:10.1007/s41365-021-00917-8
[31] B. Pechlivanovic, S. Avdic, P. Marinkovic et al., Comparison of unfolding approaches for monoenergetic and continuous fast-neutron energy spectra. Radiat. Meas. **49**, 109–114 (2013). doi:10.1016/j.radmeas.2012.12.008
[32] S.-Y. Zhang, Y.-B. Nie, Y.-Y. Ding et al., Accurate Pulse Time Distribution Determination Using MLEM Algorithm in Integral Experiments. Nucl. Eng. Technol. **57**, 103191 (2025).doi:10.1016/j.net.2024.08.060
[33] D. Schlegel, TARGET User's Manual. Physikalisch-Technische Bundesanstalt, Braunschweig, Germany (2005).
[34] Y.-B. Nie, J. Ren, X.-C. Ruan et al., The benchmark experiment on slab beryllium with D-T neutrons for validation of evaluated nuclear data. Fusion Eng. Des. **105**, 8–14 (2016). doi:10.1016/j.fusengdes.2016.01.049
[35] Y.-L. Jin, X. Tao, J.-M. Wang et al., NDplot – A plotting tool for nuclear data. EPJ Web Conf. **239**, 10004 (2020). doi:10.1051/epjconf/202023910004